Guo *et al. Cardiovascular Diabetology* (2024) 23:331
https://doi.org/10.1186/s12933-024-02404-x

Cardiovascular Diabetology

RESEARCH Open Access

MiRNA-132/212 encapsulated by adipose tissue-derived exosomes worsen atherosclerosis progression

Bei Guo[1,2], Tong-Tian Zhuang[3], Chang-Chun Li[1], Fuxingzi Li[1], Su-Kang Shan[1], Ming-Hui Zheng[1], Qiu-Shuang Xu[1], Yi Wang[1], Li-Min Lei[1], Ke-Xin Tang[1], Wenlu Ouyang[1], Jia-Yue Duan[1], Yun-Yun Wu[1], Ye-Chi Cao[1], Muhammad Hasnain Ehsan Ullah[1], Zhi-Ang Zhou[6], Xiao Lin[4], Feng Wu[5], Feng Xu[1], Xiao-Bo Liao[6*] and Ling-Qing Yuan[1*]

Abstract

Background Visceral adipose tissue in individuals with obesity is an independent cardiovascular risk indicator. However, it remains unclear whether adipose tissue influences common cardiovascular diseases, such as atherosclerosis, through its secreted exosomes.

Methods The exosomes secreted by adipose tissue from diet-induced obesity mice were isolated to examine their impact on the progression of atherosclerosis and the associated mechanism. Endothelial apoptosis and the proliferation and migration of vascular smooth muscle cells (VSMCs) within the atherosclerotic plaque were evaluated. Statistical significance was analyzed using GraphPad Prism 9.0 with appropriate statistical tests.

Results We demonstrate that adipose tissue-derived exosomes (AT-EX) exacerbate atherosclerosis progression by promoting endothelial apoptosis, proliferation, and migration of VSMCs within the plaque in vivo. MicroRNA-132/212 (miR-132/212) was detected within AT-EX cargo. Mechanistically, miR-132/212-enriched AT-EX exacerbates palmitate acid-induced endothelial apoptosis via targeting G protein subunit alpha 12 and enhances platelet-derived growth factor type BB-induced VSMC proliferation and migration by targeting phosphatase and tensin homolog in vitro. Importantly, melatonin decreases exosomal miR-132/212 levels, thereby mitigating the pro-atherosclerotic impact of AT-EX.

Conclusion These data uncover the pathological mechanism by which adipose tissue-derived exosomes regulate the progression of atherosclerosis and identify miR-132/212 as potential diagnostic and therapeutic targets for atherosclerosis.

Keywords Adipose tissue, Atherosclerosis, Melatonin, MiR-132/212, Obesity

*Correspondence:
Xiao-Bo Liao
xiaoboliaoxiangya@csu.edu.cn
Ling-Qing Yuan
allenylq@csu.edu.cn

Full list of author information is available at the end of the article

Graphical Abstract

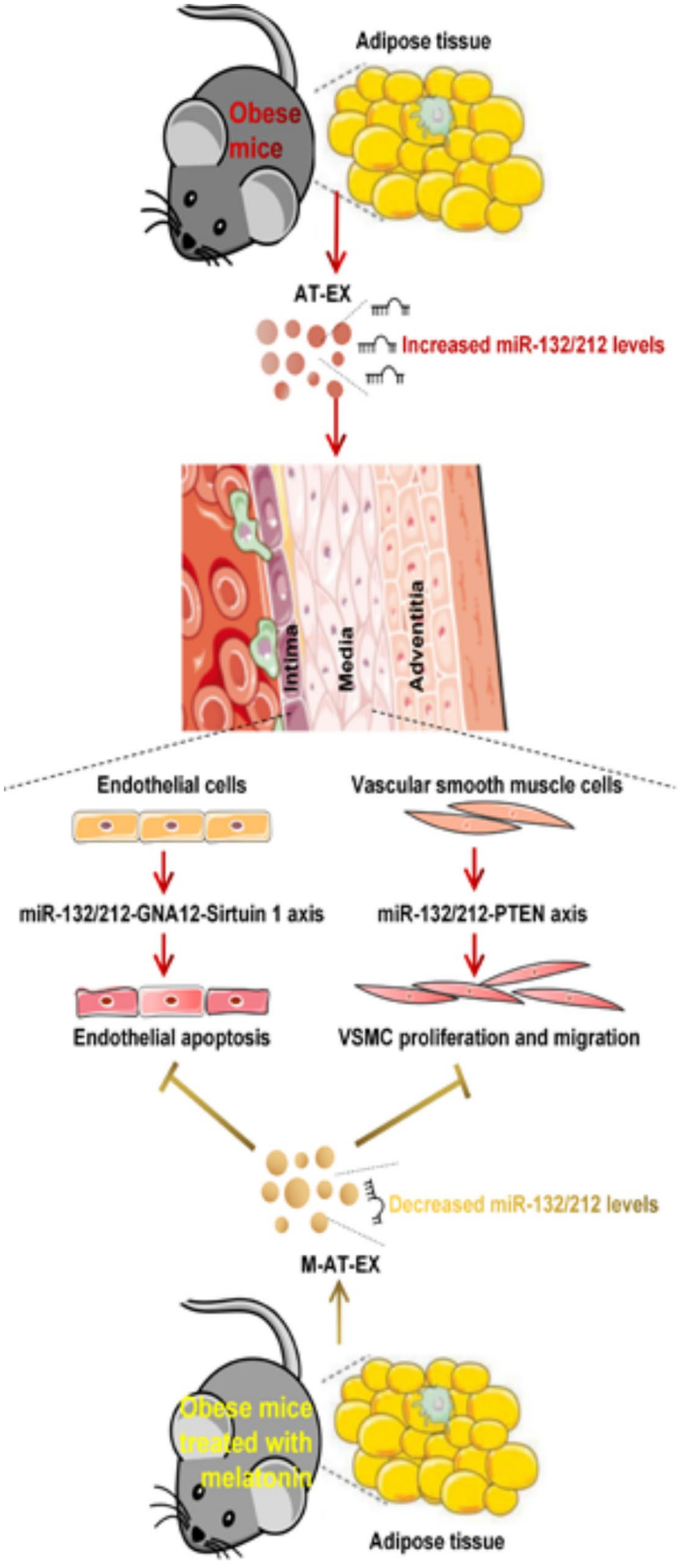

Introduction

Atherosclerosis is the primary factor increasing the occurrence of heart disease and stroke. The high global incidence and mortality rates of atherosclerotic disease place a significant economic burden [1]. Obesity is increasingly recognized as a significant risk factor for atherosclerotic disease [2]. Aberrant fat accumulation in obesity results in dysfunction in white adipose tissue [3]. Recent studies have demonstrated that visceral adipose tissue (VAT) in obese individuals is a stronger independent predictor of cardiovascular risk compared to subcutaneous adipose tissue (SAT) [4, 5].

Exosomes, which have a cup-like shape and a diameter of 40–160 nm, are secreted by all cell types and carry various biomolecules, such as DNAs, RNAs, proteins, lipids and metabolites, [6] which function in the recipient cells. For instance, adipocyte-secreted exosomal miRNA-34a promotes obesity-induced adipose inflammation, [7] adipose mesenchymal stem cell-derived exosomal miRNA-342 mitigates atherosclerosis [8] and adipose tissue macrophage-derived exosomal miRNA-155 regulates insulin sensitivity [9]. However, these studies focus on a specific type of cell-derived exosomes in adipose tissue. Adipose tissue serves as the largest endocrine organ [10–12] and is considered as one of the main sources of circulating exosomes [13]. The exosomes secreted by various cell types in adipose tissue affect the response of adjacent cells to metabolic changes, [14] indicating that adipose tissue-derived exosomes in the blood are a comprehensive reaction product of various cells in adipose tissue in response to metabolic changes. Therefore, the exosomes secreted by adipose tissue as a whole, rather than those secreted by a specific type of cells in adipose tissue, will be more valuable for studying the pathogenesis and pathophysiology of disease. Recently, more and more researchers have paid attention to this key point. For example, brown adipose tissue-derived exosomes have been reported to alleviate the metabolic syndrome, [15] and visceral adipose tissue-derived exosomes, to exacerbate colitis [16]. Notably, a novel study has reported that VAT-EX exacerbate atherosclerosis by enhancing macrophage foam cell formation [17]. However, it is still unclear which active molecules function in these exosomes and whether VAT-EX affects arterial endothelial apoptosis and the proliferation and migration of VSMCs in atherosclerosis.

Melatonin, a crucial hormone secreted by the pineal gland, was initially believed to regulate circadian rhythms [18]. Extensive evidence indicates that melatonin has potent antioxidative and anti-inflammatory properties [19, 20]. As for atherosclerosis, the intragastric administration of melatonin markedly reduced the amount of plaque in the aorta, [21] where melatonin receptors exist [22, 23], suggesting a direct protective role of this molecule in atherosclerosis. Additionally, melatonin may play an indirect role in alleviating atherosclerosis by reducing weight gain and enhancing other metabolic processes in both animal models and humans [24]. Recently, a new study reported that melatonin attenuates adipose inflammation by changing the cargo carried by adipose-derived exosomes [25]. However, data regarding the effect of melatonin on atherosclerosis by changing the inflammatory miRNA profile in adipose-derived exosomes are scarce. In this present study, our aim is to explore whether melatonin alleviates the atherogenic impact of adipose-derived exosomes by altering the profile of inflammatory miRNAs and to identify the key effector molecules within these exosomes for identifying potential diagnostic and therapeutic targets in atherosclerosis.

Materials and methods

Establishment of diet-induced obesity (DIO) mouse model

All animal experiments comply with the ARRIVE guidelines. All mice were housed in a specific pathogen-free environment with a 12-h light-dark cycle and 40–60% humidity at 18–23 °C in the Second Xiang-Ya Hospital. Six-week-old C57BL/6J male mice were fed with a 60% high-fat diet (D12492; Research Diets, Inc.) for 16 weeks to induce a mouse model of obesity ($N=40$, five mice per cage). All mice were fed with the high-fat diet until the end of the experiment, and half of them were selected to receive drinking water supplemented with 0.4 mg/mL melatonin (Sigma-Aldrich, M5250) for the next 6 weeks at the 10th week of high-fat diet (HFD) intervention using a random number table. The drinking water bottle was wrapped in tin foil to prevent light-induced degradation of melatonin. Obesity was assessed as in a previous study [16]. Body weight was measured weekly, and daily food consumption was recorded. Glucose and insulin tolerance tests were performed as previously described [26].

Establishment of atherosclerosis mouse models

Apolipoprotein E knockout male mice ($ApoE^{-/-}$ mice; B6/JGpt-Apoeem1Cd82/Gpt; Strain No. T001458) were purchased from GemPharmatech (Nanjing, China). All $apoE^{-/-}$ mice were fed with a high-fat diet containing 1.25% cholesterol and 40% fat for 12 weeks (D12108C; Research Diets, Inc.). At the 6th week after a high-fat diet, mice were randomly divided into five groups by flipping a coin and were injected with PBS or exosomes through caudal vein (20 in each group, five mice per cage), twice a week. No mice died during the trial period.

Isolation of exosomes from adipose tissue

Mice were euthanized with 100% CO_2 inhalation after gas anesthesia with inhaled isoflurane (5%). Exosomes were isolated from adipose tissue as previously described

[14, 16]. Briefly, anesthetized DIO mice were perfused through the heart at the left ventricle with PBS to remove blood from the tissue. The VAT (epididymal adipose tissue) and SAT (inguinal adipose tissue) were aseptically dissected from the DIO mice, cut into small pieces and then cultured in serum-free Dulbecco's Modified Eagle Medium for 24 h. The supernatant was collected and centrifuged at 600×*g* for 5 min to remove and discard the floating adipocytes. The supernatant was centrifuged at 1200×*g* at 4 °C for 15 min to remove cellular debris and then centrifuged again at 10,000×*g* at 4 °C for 15 min to remove large extracellular vesicles. The resulting supernatant was then filtered through a 0.22-μm filter (Merck Millipore) to remove any contaminating microvesicles and any remaining cellular debris. The clarified supernatant was then concentrated to 250 μL in 100 KD MWCO Amicon Ultra-15 centrifugal filter units and diluted to 10 mL in PBS. Samples were then centrifuged at 100,000×*g* at 4 °C for 1.5 h to pellet small extracellular vesicles. The resulting pellet was resuspended in PBS and centrifuged again at 100,000×*g* at 4 °C for 1.5 h. The final pellet was resuspended in PBS, which was used for exosome identification or stored at −80 °C for subsequent functional experiments.

Identification of exosomes derived from adipose tissue

For size distribution analysis, exosomes were diluted (1 ug/uL at protein concentration) and subjected to NanoSight (Malvern, UK). The exosomal morphology was observed by transmission electron microscopy (JEM-2000EX TEM, Japan). The expression of exosome markers was analysed by western blotting.

Exosome labelling and tracking in vivo and ex vivo

Exosomes were labelled with DiR (Invitrogen) according to our previous study [27]. Free dyes were removed by ultracentrifugation at 100,000×*g* at 4 °C for 1.5 h. DiR-labelled exosomes (100–125 μg) were injected into mice through the caudal vein. Exosome localization in the whole body and individual organs was detected by an IVIS SPECTRUM (PerkinElmer, US) 12 h after injection. For analysis of sliced sections, the fresh aorta tissue was dissected, washed and embedded in an optimal cutting temperature compound.

Exosomes were labelled with the PKH26 Red Fluorescent Cell Linker Kit according to the manufacturer's protocol. Labelled exosomes were incubated with bEnd.3 and VSMCs for 12 h and detected by confocal laser scanning microscopy (Olympus, Japan). Antibodies used were anti-α-SMA (Servicebio, GB111364), anti-CD31 (Servicebio, GB113151), anti-TSG101 (Abcam, ab125011) and the corresponding secondary antibody (Servicebio, 23303, GB27303).

Oil Red O staining and Masson's trichrome staining

After 4% paraformaldehyde perfusion, the adventitia was carefully removed under the microscope, and then the aorta was dissected longitudinally to expose the intimal surface for Oil Red O staining (Sigma-Aldrich, O-0625), referring to a previous study [27]. Frozen cross-sections of the aortic root were prepared for Oil Red O staining and Masson's trichrome staining, and lesion quantification was performed using Image J (NIH) as previously described [28].

Cell culture and transfection

The immortalized mouse endothelial cell line bEnd.3 was cultured in DMEM (4.5 g/L glucose) basic medium supplemented with 10% foetal bovine serum (FBS) (ExCell Bio, FSD500). bEnd.3 were treated with 0.4 mmol/L palmitate acid (PA) (Sigma, P5585) to induce cell apoptosis. Primary VSMCs were purchased from CHI Scientific and cultured in DMEM (4.5 g/L glucose) basic medium supplemented with 10% FBS (Gibco, 10099-141). Primary VSMCs were treated with 50 ng/mL PDGF-BB (PeproTech, 100-14B-2) to induce cell proliferation and migration. Cells were maintained at 37 °C with 5% CO_2 in a humidified environment and passaged when confluent.

The bEnd.3 or VSMCs were seeded in 6-well plates until they reached 60% confluence, and then the cells were transfected following the instructions accompanying the siRNA-mate reagent (GenePharma, 190903). At 24 h after transfection, bEnd.3 were exposed to PA for 24 h, and VSMCs were exposed to PDGF-BB for the next 24 h. The miR-132/212 mimics were purchased from Ribo (Guangzhou, China), including miR10000144, miR10000659, miR10000269, miR10000426 and miR1N0000001-1-5. Gna12-specific small interfering RNA (siRNAs) were synthesized by GenePharma (Shanghai, China), including Gna12-Mus-678 (sense: GGAUA ACUUGGACCGGAUUTT, and antisense: AAUCCGG UCCAAGUUAUCCTT); Gna12-Mus-1186 (sense: GC CAUAGACACCGAGAACATT, and antisense: UGUUC UCGGUGUCUAUGGCTT); Gna12-Mus-935 (sense: G GCUGGUGGAGUCCAUGAATT, and antisense: UUC AUGGACUCCACCAGCCTT) as well as si-NC. PTEN-homo-1731 (sense: CGGGAAGACAAGUUCAUGUT T, and antisense: ACAUGAACUUGUCUUCCCGTT); PTEN-homo-1567 (sense: GCUACCUGUUAAAGAAU CATT, and antisense: UGAUUCUUUAACAGGUAGCT T); PTEN-homo-1425 (sense: GGUGUAAUGAUAUGU GCAUTT, and antisense: AUGCACAUAUCAUUACAC CTT). Additionally, AntagomiRs, including AntagomiR-NC and AntagomiR-132/212, were procured from GenePharma (Shanghai, China). VAT-EX were transfected with AntagomiRs at a concentration of 200 nM for 1 h at 37 °C. Untransfected AntagomiRs were eliminated through centrifugation at 4000×*g* for 5 min using a

100 kDa Amicon Ultra-4 Centrifugal Filter Unit (Merck Millipore) [26]. The transfection efficiency in VAT-EX was evaluated using qRT-PCR.

Cell counting kit-8 (CCK-8) assay and EdU assay

The CCK-8 kit (Dojindo, Tokyo, Japan) was used to measure cell viability according to the manufacturer's protocol. Briefly, the bEnd.3 and VSMCs were seeded in 96-well plates, and the living cells were quantified by incubation with CCK-8 reagent for 4 h at the indicated time of exosome treatment. Optical density values at 450 nm were measured using a microplate reader (NanoDrop 2000). For EdU (Sangon Biotech, E607204) analysis, the nucleus was counterstained with DAPI (Servicebio, G1012), and the EdU-positive images were captured by fluorescence microscopy (Nikon, Japan).

VSMCs migration analysis

Transwell assay inserts (8 μm) were placed into a 24-well plate (Corning, 3422). After 48 h of incubation with exosomes, non-migrated VSMCs were carefully removed by cotton swabs. Migrated cells were fixed with methanol and stained with crystal violet (0.1%). The cells on the bottom side of the membrane were observed and counted with a phase-contrast microscope (Nikon, Japan).

Flow cytometry analysis of cell apoptosis

Apoptosis was detected by using the Annexin V-FITC Apoptosis Detection Kit (BD, 556547). EDTA-free trypsin-digested cells were washed with PBS and resuspended in 150 μL of 1× binding buffer, and then 5 μL of Annexin V-FITC and 5 μL of propidium iodide were added. After 15 min incubation in the dark, apoptosis was detected with a flow cytometer (BD Biosciences, USA), and data analysis was conducted using FlowJo software (Stanford University, USA).

Dual-luciferase reporter assay

The target genes of miR-132/212-3p were identified using TargetScan, RNAInter, ENCORI, and RGD databases. Luciferase reporter vectors, including pmiR-report-Gna12 WT and pmiR-report-Gna12 Mut, or pmiR-report-PTEN WT and pmiR-report-PTEN Mut, were separately transfected into cells with miR-132 or miR-212 mimics. After 24 h of transfection, the cells were collected and lysed. Firefly luciferase activity and Renilla luciferase activity were measured using the Dual-Luciferase Reporter Assay System (Promega, USA).

Blood pressure and lipid profile analysis

Blood pressure was tested by tail cuff measurements using the BP-2000 Blood Pressure analysis system (Visitech Systems) according to the manufacturer's instructions. Lipid profile analysis were performed at sacrifice. Total cholesterol and triglyceride levels were detected using the Infinity™ Cholesterol Reagent and Infinity™ Triglycerides Liquid Stable Reagent (Thermo Scientific) according to the manufacturer's instructions. HDL-cholesterol and LDL-cholesterol were measured by colorimetric assay using HDL and LDL cholesterol Assay Kit (Abcam, Cambrige, England, UK).

TUNEL staining and immunofluorescence assays

For TUNEL and CD31 double staining, the In Situ Cell Death Detection kit (Roche, 11684795910), anti-CD31 (Servicebio, GB113151) and Cy3-conjugated Goat Anti-Rabbit IgG (Servicebio, GB21303) were used on paraffin-embedded aorta sections according to the manufacturer's instructions. For α-SMA and PCNA co-staining, aorta sections were incubated with anti-α-SMA (Servicebio, GB111364) and anti-PCNA (Proteintech, Cat No. 60097-1-Ig) followed by the detection of Alexa Fluor®488-conjugated Goat Anti-rabbit IgG (Abcam, ab150077) and Cy3-conjugated Goat Anti-Mouse IgG (Servicebio, GB21301). The sections were observed under a fluorescence microscope (Nikon).

qRT-PCR

The exosomes, cells or aorta were homogenized in TRIzol (Invitrogen). RNA was isolated according to the manufacturer's protocol, and its quality and concentration were determined from the absorbance at 260 nm, 280 nm and 230 nm. cDNA was prepared by reverse transcribing 1 μg of RNA with the Mir-X miRNA First-Strand Synthesis Kit (638315, TKA) or PrimeScript RT reagent Kit with gDNA Eraser (RR047A, TKA). qRT-PCR was performed with TB Green (RR820A, TKA). The ΔΔCt method was used for miRNA quantification relative to U6 levels. The PCR primers were purchased from Genecopoeia (U6, MmiRQP9002; mmu-mir-155-5p, MmiRQP0890; mmu-mir-146a-5p, MmiRQP0196; mmu-mir-181a-5p, MmiRQP0232; mmu-mir-21a-5p, MmiRQP0316; mmu-mir-132-3p, MmiRQP0161; mmu-mir-212-3p, MmiRQP0931; mmu-mir-29a-3p, MmiRQP0371). The following primers were provided by Sangon Biotech (Shanghai, China): *Gna12* forward 5-ACCATCTTCGA CAACATCCTTA-3, reverse 5-CTCGAAGGCCATCAG AAACATC-3; *PTEN* forward 5-GACCAGAGACAAAA AGGGAGTA-3, reverse 5-ACAAACTGAGGATTGCA AGTTC-3.

Western blot

Protein was extracted from cells or aorta by homogenization in RIPA buffer (Beyotime Biotechnology, China) supplemented with the protease inhibitor cocktail (Bimake, B14001). The gel lanes were loaded with equal quantities of protein, which were separated by SDS-PAGE and transferred to a PVDF membrane. After blocking with

5% skim milk, the PVDF membrane was then incubated overnight at 4 °C with primary antibodies. Antibodies used were anti-CD81 (Abcam, ab79559), anti-CD9 (Abcam, ab92726), anti-TSG101 (Abcam, ab125011), anti-GNA12 (Abcam, ab154004), anti-PTEN (CST, #9559), anti-cleaved-caspase3 (CST, #9664T), anti-Bax (CST, #2772T), anti-Bcl-2 (CST, #3498T), anti-PNCA (Proteintech, 10205-2-AP) and anti-GAPDH (Proteintech, 10494-1-AP). Then, the PVDF membrane was incubated with the corresponding secondary antibodies. The bands were visualized using the ECL detection reagent (Immobilon, WBKLS0500).

Statistical analysis

All data are expressed as the mean ± SD. Statistical significance was analysed by GraphPad Prism 9.0 using an unpaired two-sided Student's *t*-test or one-way analysis of variance with LSD or Bonferroni correction for multiple comparisons. Differences with $P<0.05$ were considered statistically significant.

Results

Distribution of adipose tissue-derived exosomes in mice

High-fat diet-induced obesity in mice was demonstrated by a significant increase in body weight and a decline in glucose tolerance, as illustrated in Fig. S1A–C. To investigate the potential impact of AT-EX from obese mice on the development of atherosclerosis, exosomes were isolated and purified from SAT and VAT. These isolated exosomes exhibited the characteristic morphology of exosomes when observed under the transmission electron microscope (Fig. 1A) and expressed the exosomal markers CD9, CD81, and TSG101 (Fig. 1B). The nanoparticle tracking analysis provided additional validation of the exosomes' identity (Fig. 1C). The data demonstrate that we isolated the AT-EX successfully.

To examine the distribution of AT-EX in vivo, exosomes were labeled with DiR (infrared fluorescence dye DiOC18) for tracking via in vivo and ex vivo fluorescence imaging (Fig. 1D–G). Following intravenous injection, DiR-labeled exosomes were observed to accumulate significantly in the aorta 12 h later (Fig. 1D, E). Interestingly, our data revealed that the largest share of exosomes accumulated in the liver. Furthermore, we found

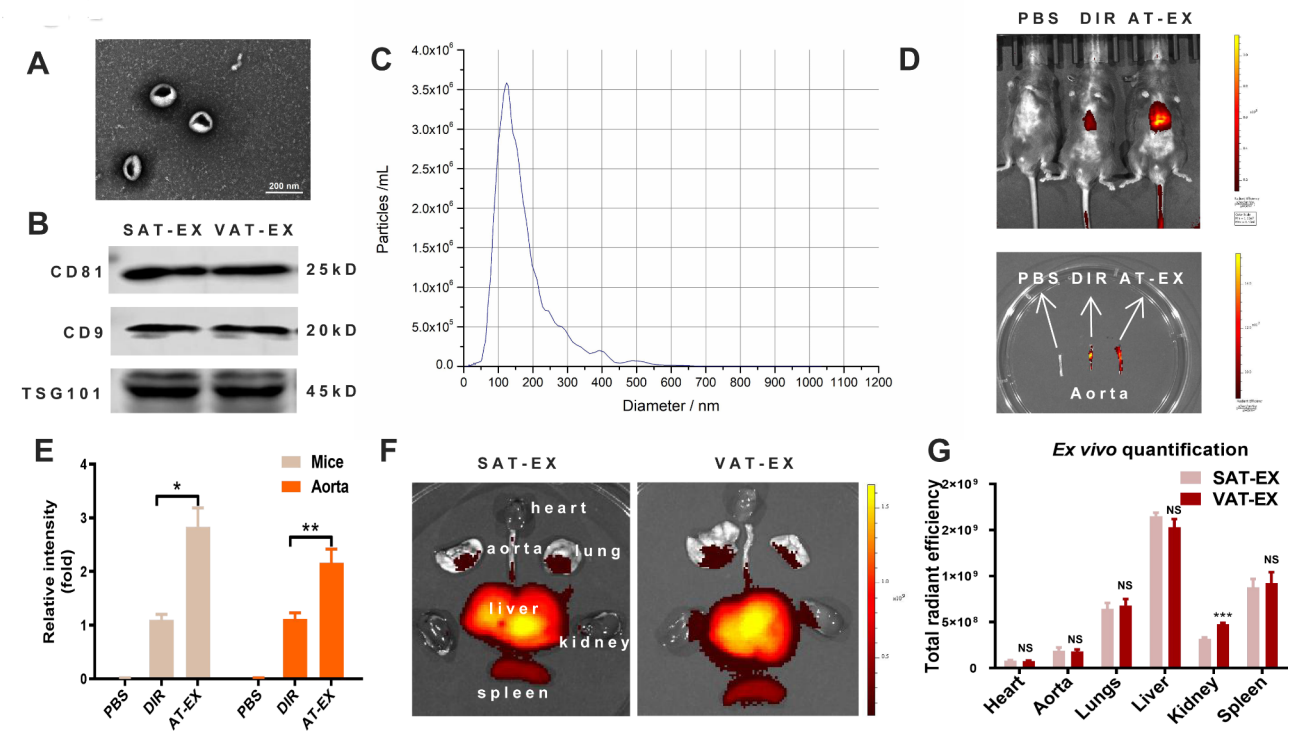

Fig. 1 Identification of AT-EX and uptake of DiR-labelled AT-EX in the aortas of apoE$^{-/-}$ mice. **A** Representative image of the ultrastructure of adipose tissue exosomes (AT-EX) observed by transmission electron microscopy, scale bar = 200 nm. **B** Expression of exosome markers (CD81, CD9 and TSG 101) in exosomes derived from subcutaneous adipose tissue (SAT) and visceral adipose tissue (VAT) in diet-induced obese mice (DIO). **C** The average particle size distribution of AT-EX using nanoparticle tracking analysis. **D** Approximately 100 μg (at protein level) in 100 μL of AT-EX labelled with DiR was injected via tail vein. Fluorescence images of the mice in vivo and the aorta ex vivo were obtained 12 h after intravenous injection. **E** Quantification of D. **F** Distribution of other organs ex vivo after DiR-labeled AT-EX injection. **G** Quantification of F. ***$P<0.001$. Data are represented as mean ± SD

no significant difference in the tissue distribution of SAT and VAT-derived exosomes (Fig. 1F, G).

AT-EX from obese mice contributes to aggravated atherosclerosis in vivo

Exosomes secreted from various adipose tissue types exhibit distinct functions [15, 16, 27]. In our study, the effects of SAT-derived exosomes (SAT-EX) and VAT-derived exosomes (VAT-EX) from obese mice on atherosclerosis were investigated. Firstly, we treated mice in accordance with the procedures shown in Fig. 2A. Treatment with VAT-EX significantly increased the number of en face and cross-sectional atherosclerotic lesions in apoE$^{-/-}$ mice, while SAT-EX showed a slight increase compared to the vehicle group (Fig. 2B, C). Importantly, VAT-EX significantly augmented the apoptosis of ECs and the proliferation and migration of VSMCs compared to the vehicle group (Fig. 2D–G). In addition, Neither SAT-EX nor VAT-EX had effects on lipid levels including total cholesterol, triglyceride, low-density lipoprotein, and high-density lipoprotein or collagen synthesis around atherosclerotic lesions (Fig. S2; Table S1). Collectively, these data revealed that AT-EX aggravates the progression of atherosclerosis at least in part via accelerating the apoptosis of ECs and the proliferation and migration of VSMC.

AT-EX from obese mice aggravates endothelial apoptosis, VSMC proliferation and migration in vitro

Further, we verified the effects of SAT-EX and VAT-EX on ECs and VSMCs in vitro. Initially, the internalization of exosomes in bEnd.3 (a mouse endothelial cell line) was observed. As shown in Fig. 3A, PKH-26-labeled AT exosomes (red fluorescence) could be internalized by bEnd.3 (CD31 positive, green fluorescence) following 12 h of co-incubation. Cell activity detection displayed that VAT-EX mildly reduced the proliferation of bEnd.3 at 24 h compared to the vehicle group (Fig. 3B). Subsequently, a cell model of endothelial apoptosis induced by PA [28–30] was established to mimic in vivo lipotoxicity. Consistently, PA treatment for 8 h and 12 h significantly increased the expression of cleaved-caspase 3, a key apoptotic protein in bEnd.3 (Fig. 3C). Moreover, we illustrated that VAT-EX (at concentrations of 50, 100, and 200 μg/mL) significantly elevated cleaved-caspase3 expression in PA-induced bEnd.3 after 12 h of treatment compared to the PA group, while a high dose of SAT-EX (at concentrations of 100 and 200 μg/mL) also demonstrated a mild facilitation of apoptosis (Fig. 3D). Therefore, an exosome concentration of 100 μg/mL was selected for follow-up experiments. The anti-apoptotic protein Bcl-2 and the pro-apoptotic protein Bax are two important participants in the apoptosis signaling pathway [28]. As anticipated, western blot analysis revealed a moderate decrease in the Bcl-2/Bax ratio in the VAT-EX group compared to the PA group (Fig. 3E). Accordingly, flow cytometry analysis of apoptosis further confirmed the pro-apoptotic effect of VAT-EX in PA-induced bEnd.3 (Fig. 3F).

Then, primary aortic VSMCs were identified by using the cell marker α-SMA (Fig. S3). PKH-26-labeled AT exosomes (red fluorescence) were internalized efficiently by VSMCs (α-SMA positive, green fluorescence) (Fig. 3G). Cell activity detection displayed that SAT-EX only slightly augmented VSMC proliferation on treatment day 2, but VAT-EX significantly enhanced VSMC proliferation compared to the PDGF-BB group (Fig. 3H, I). The transwell assay showed that compared to the PDGF-BB group, VAT significantly enhanced VSMC migration (Fig. 3J). As expected, VAT-EX significantly increased PCNA expression, a key protein regulator of cell proliferation, in PDGF-BB-induced VSMCs compared to the PDGF-BB group (Fig. 3K). Together, these data reveal that AT-EX enhances endothelial apoptosis and the proliferation and migration of VSMCs in vitro.

Increased expression of the miR-132/212 cluster in the VAT-EX from obese mice

Previous research has shown that numerous miRNAs, including miR-132, miR-212, miR-29a, miR-181a, miR-155, miR-21a, and miR-146a, are key players in inflammation-related disorders [31–36]. Thus, we assessed the expression profiles of these miRNAs using qRT-PCR and observed that the average levels of these miRNAs were usually higher in VAT-EX compared to SAT-EX. However, the most notable increase was observed in the miR-132/212 cluster in VAT-EX, particularly miR-132 (Fig. 4A). To assess whether the mature miR-132/212 found in target cells originates from AT exosomes, we simultaneously detected both primary and mature miR-132/212. Treatment with VAT-EX significantly augmented the level of mature miR-132/212, and treatment with SAT-EX slightly elevated the level of mature miR-132/212 in bEnd.3 and VSMCs, but not primary miR-132/212 (Fig. S4A–H), demonstrating that the increase of miR-132/212 level in target cells is due to the delivery of exosomes rather than endogenous production.

Interestingly, the miR-132/212 level is significantly lower in SAT-EX compared to VAT-EX in DIO mice. Why does SAT-EX still exhibit atherogenic properties? Furthermore, we assessed the differential expression of miR-132/212 in AT-EX derived from lean mice fed a normal chow (NC) diet and DIO mice fed a high-fat diet. The level of miR-132/212 in SAT-EX from DIO mice was significantly elevated compared to that in SAT-EX from normal mice (Fig. S5A). Similarly, the level of miR-132/212 in VAT-EX of DIO mice was greatly higher than that in VAT-EX of normal mice (Fig. S5A). Additionally, injection with DIO-SAT-EX significantly increased

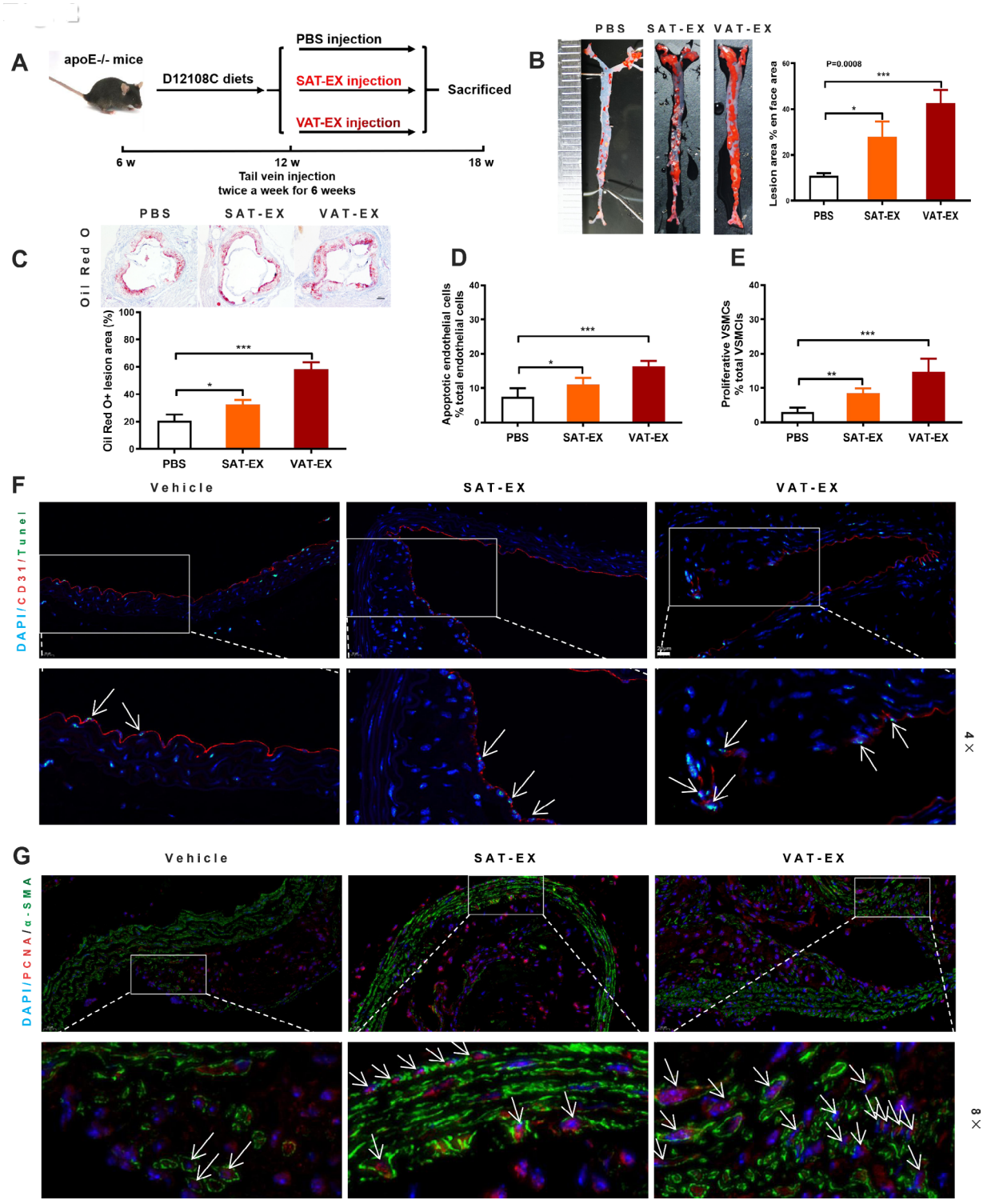

Fig. 2 AT-EX from obese mice aggravate atherosclerosis by augmenting endothelial apoptosis and the proliferation and migration of VSMCs in apoE$^{-/-}$ mice. **A** The animal experimental procedure for detecting the effects of SAT exosomes or VAT exosomes treatments on atherosclerosis (AS). **B** Representative images showing Oil Red O staining (red) of neutral lipids in en face atherosclerotic lesions and the quantification, $N = 6$. **C** Representative micrographs showing Oil Red O staining of neutral lipids in the aortic root 300 μm from the aortic sinus and the quantification (scale bar = 200 μm, $N = 6$). **D** The percentage of apoptotic ECs in the thoracic aorta. **E** The percentage of proliferative VSMCs in the thoracic aorta. **F** Representative images of TUNEL (apoptotic cells, green) and CD31 (red) co-staining in sections of thoracic aortas, arrowheads show TUNEL/CD31 co-localization, scale bar = 20 μm, $N = 6$. **G** Representative images of α-SMA (green) and PCNA (red) co-staining in sections of thoracic aortas, arrowheads and dotted line show α-SMA/PCNA co-localization, scale bar = 20 μm, $N = 5$. *NS* no significance, $^{*}P < 0.05$, $^{**}P < 0.01$, $^{***}P < 0.001$. Data are represented as mean ± SD

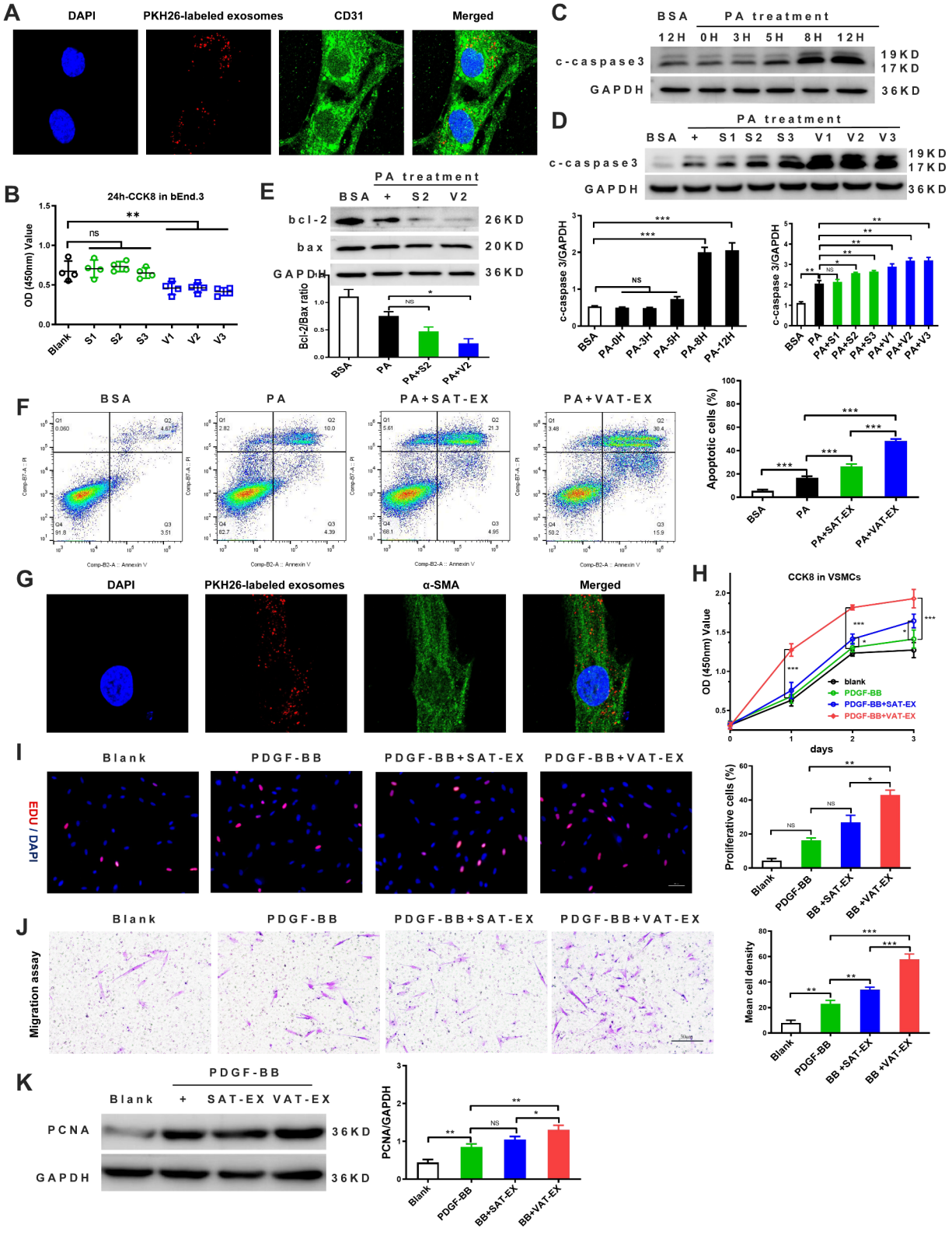

Fig. 3 (See legend on next page.)

(See figure on previous page.)

Fig. 3 AT-EX from obese mice exacerbates endothelial apoptosis and the proliferation and migration of VSMC in vitro. **A** Representative confocal micrograph of PKH-26-labelled exosomes (red) internalized by bEnd.3 (CD31 positive, green). **B** The effect of SAT-EX and VAT-EX on the viability of bEnd.3 at 24 h (S1, S2 and S3 represent 50 μg/mL, 100 μg/mL and 200 μg/mL SAT-EX, respectively; V1, V2 and V3 show 50 μg/mL, 100 μg/mL and 200 μg/mL VAT-EX, respectively). **C** Expression of c-caspase 3 at different time after palmitic acid (PA, 0.4 mmol/L) treatment. **D** Expression of c-caspase3 in PA-induced bEnd.3 after 12 h of AT-EX (SAT-EX or VAT-EX) treatment. **E** Protein levels of BCL-2 and Bax in PA-induced bEnd.3 after AT-EX treatment. **F** Apoptotic bEnd.3 were stained with Annexin V-FITC and propidium iodide (PI). **G** Representative confocal micrograph of PKH-26-labelled exosomes (red) internalized by primary VSMCs. **H** Effect of AT-EX on the viability of primary VSMCs. **I** Representative proliferation images of primary VSMCs, scale bar = 50 μm. **J** Representative migration images of primary VSMCs, scale bar = 50 μm. **K** PCNA expression in PDGF-BB-induced primary VSMCs after AT treatment. *NS* no significance, $^{*}P < 0.05$, $^{**}P < 0.01$, $^{***}P < 0.001$, $N = 6$ independent experiments. Data are represented as mean ± SD

the en face and cross-sectional atherosclerotic lesions in apoE$^{-/-}$ mice compared to the NC-SAT-EX group (Fig. S5B–D). Similarly, DIO-VAT-EX injection greatly increased the en face and cross-sectional atherosclerotic lesions in apoE$^{-/-}$ mice compared to the NC-VAT-EX group (Fig. S5B–D). Moreover, treatment with NC-VAT-EX didn't have a significant effect on the development of atherosclerosis in apoE$^{-/-}$ mice compared to the NC-SAT-EX group (Fig. S5B–D). Consistent with in vivo data, treatment with DIO-SAT-EX significantly enhanced the expression of C-caspase3 in ECs and PCNA in VSMCs, and promoted the migration of VSMCs compared to the NC-SAT-EX group (Fig. S5E–G). Meanwhile, treatment with DIO-VAT-EX largely increased the protein level of C-caspase3 in ECs and PCNA in VSMCs, and promoted the migration of VSMCs compared to the NC-VAT-EX group (Fig. S5E–G). Therefore, these results suggest that miR-132/212 play a role in obese mice VAT and SAT exosomes- mediated atherosclerosis exacerbation.

Exosomes encapsulating miR-132/212 aggravate endothelial apoptosis through targeting Gna12 and promote VSMCs proliferation and migration via targeting PTEN

To study the underlying regulatory mechanisms of exosome encapsulation of miR-132/212, we used four databases to predict the target gene of miR-132/212 (Fig. 4B). The bioinformatic score system showed that Gna12 has binding sites for miR-132/212 (Fig. 4C). Transfection alone or co-transfection of miR-132/212 down-regulated the mRNA and protein levels of Gna12 in bEnd.3 (Figs. 4D, S6A), increasing endothelial apoptosis (Fig. 4E). To verify these results, we created a luciferase reporter with a mutant Gna12 3′UTR containing the miR-132/212-binding site at the seed sequence (Fig. 4F). Luciferase reporter assays confirmed that miR-132/212 effectively targets the wild-type Gna12 3′UTR (Fig. 4F). Subsequently, we identified a small interfering RNA with superior silencing efficiency, siGna12-3 showing more effectiveness than the other candidates (Figs. 4G, S6B). Consistent with the aforementioned results, GNA12 silencing enhanced the expression of c-caspase 3 in ECs (Fig. 4H). These results suggest a role for miR-132/212 in AT-EX-mediated endothelial apoptosis through direct Gna12 targeting in ECs.

Recent studies have reported that the miR-132/212 cluster directly targets PTEN [37, 38], which plays a critical role in regulating cell proliferation and migration [39, 40]. Consistent with this, transfection of miR-132/212 mimics, alone or in combination, led to a reduction in PTEN mRNA and protein levels in VSMCs (Figs. 4I, S7), thereby promoting VSMC proliferation and migration (Fig. 4J–L). Furthermore, luciferase reporter assays confirmed the effective targeting of wild-type PTEN 3′UTR by miR-132/212 (Fig. 4M). We further knocked down PTEN using siRNA (Figs. 4N, S7) and found that interfering PTEN increased the expression of PCNA in VSMCs (Fig. 4O). These results underscore the significance of exosome-encapsulated miR-132/212 in targeting PTEN within VSMCs.

AntagomiR-132/212 counteracts pro-atherosclerotic effects of VAT-EX from obese mice

To ascertain the direct involvement of miR-132/212 in promoting endothelial apoptosis and VSMC proliferation and migration, specific AntagomiRs were employed to silence miR-132/212 in VAT-EX. Following transfection with AntagomiR-132/212, a substantial decrease in miR-132/212 expression within VAT-EX was observed (Fig. 5A). Subsequently, bEnd.3 cells treated with VAT-EX + AntagomiR-132/212 exhibited reduced cleaved-caspase 3 expression compared to those treated with VAT-EX + AntagomiR-NC (Fig. 5B). Moreover, VSMCs treated with VAT-EX + AntagomiR-132/212 demonstrated decreased proliferation and migration compared to those treated with VAT-EX + AntagomiR-NC (Fig. 5C–E). In vivo, the VAT-EX-treated apoE$^{-/-}$ mice were randomly divided into two groups: VAT-EX + AntagomiR-NC and VAT-EX + AntagomiR-132/212. Mice treated with VAT-EX + AntagomiR-132/212 showed reduced the number of en face and cross-sectional atherosclerotic lesions compared to the VAT-EX + AntagomiR-NC group (Fig. 5F–G). Correspondingly, Mice treated with VAT-EX + AntagomiR-132/212 displayed decreased endothelial apoptosis, VSMC proliferation and migration compared to the VAT-EX + AntagomiR-NC group (Fig. 5H–K). Overall, AntagomiR-132/212 mostly counteracted the pro-atherosclerotic effects induced by VAT-EX through increasing endothelial cell apoptosis and VSMC proliferation and migration.

Melatonin alleviates pro-atherosclerotic effects of exosomes derived from obese mice AT via targeting the miR-132/212-GNA12/PTEN signaling pathway in apoE$^{-/-}$ mice

Previous studies have highlighted the potent anti-inflammatory properties of melatonin in adipose tissue [25, 41]. However, it remains uncertain whether melatonin modifies the composition of adipose tissue-derived exosomes to indirectly impede atherosclerosis progression. In alignment with prior research, melatonin treatment induced weight loss in HFD-fed mice without affecting food intake (Fig. S8). Subsequently, SAT-derived exosomes (M-SAT-EX) and VAT-derived exosomes (M-VAT-EX) from obese mice treated with melatonin were intravenously administered to apoE$^{-/-}$ mice to investigate their atherogenic effects (Fig. 6A). M-VAT-EX still moderately increased the en face and cross-sectional atherosclerotic lesions in apoE$^{-/-}$ mice compared to the vehicle group, whereas the atherogenic effect of M-VAT-EX was significantly weakened when compared to the VAT-EX group (Fig. 6B, C), probably correlated with still higher miR-132/212 levels in M-VAT-EX (Fig. S9A, B). Interestingly, M-SAT-EX mitigated the atherosclerotic lesions compared to the vehicle group (Fig. 6B, C), possibly implicated with some other unexplored mechanism. What's more, the miR-132/212 level in the M-SAT-EX-treated aorta was equivalent to that in the NC-SAT-EX-treated aorta, while its levels in the M-VAT-EX-treated aorta was significantly higher than that in the NC-VAT-EX-treated aorta (Fig. S9C, D). As expected, M-VAT-EX only slightly increased endothelial apoptosis and the proliferation and migration of VSMCs compared to the vehicle group, while M-SAT-EX alleviated these compared to the SAT-EX group (Fig. 6D–G). Additionally, no significant differences were observed in the amounts of collagen surrounding atherosclerotic lesions and lipid levels across the four groups (Fig. S10A, B; Table S2). Finally, we sought to verify the involvement of miR-132/212-GNA12/PTEN signaling in vivo. In comparison to the vehicle group, both VAT-EX and SAT-EX notably reduced the levels of Gna12 and PTEN in the aorta; however, the impact of VAT-EX was more pronounced than that of SAT-EX. In contrast, M-SAT-EX restored the expression of Gna12 and PTEN in the aorta, while M-VAT-EX only slightly decreased the level of PTEN and exhibited a tendency to decrease Gna12 levels (Fig. S11A–C). Collectively, these data reveal that melatonin attenuates the pro-atherosclerotic effect of VAT and SAT exosomes derived from obese mice, probably associated with miR-132/212-GNA12/PTEN signaling.

The endothelial miR-132/212-Gna12 axis and medial miR-132/212-PTEN axis are indispensable for the effects of AT-EX on atherosclerosis

To investigate the potential association between inflammatory miRNA alterations in exosomes and the underlying mechanism, the expression of these miRNAs was analyzed in four types of AT-EX exosomes (SAT-EX, VAT-EX, M-SAT-EX, and M-VAT-EX) using qRT-PCR. The miRNA spectrum associated with atherosclerosis was generally diminished in AT-EX exosomes from obese mice treated with melatonin, especially miR-132/212 (Fig. 7A, B). Subsequently, the effects of M-SAT-EX and M-VAT-EX on ECs and VSMCs were assessed. Cell viability analysis revealed no significant impact on bEnd.3 proliferation upon treatment with M-SAT-EX and M-VAT-EX compared to the control group (Fig. 7C). Notably, M-VAT-EX slightly increased the levels of mature miR-132/212 in bEnd.3 compared to M-SAT-EX, but not primary miR-132/212 in bEnd.3 (Fig. S12A–D). As expected, M-VAT-EX induced a moderate increase in apoptotic cell proportion and c-caspase 3 expression in bEnd.3, whereas M-SAT-EX alleviated these effects (Fig. 7D, E). Consistently, M-VAT-EX reduced GNA12 expression and the Bcl-2/bax ratio, while M-SAT-EX rescued these effects (Fig. 7E). Furthermore, in VSMCs, M-VAT-EX slightly elevated the level of mature miR-132/212 compared to M-SAT-EX, while primary miR-132/212 levels were similar (Fig. S12E–H). The proliferation and migration of VSMCs were enhanced by M-VAT-EX but hindered by M-SAT-EX, compared to the PDGF-BB group (Fig. 7F–J). M-VAT-EX increased the expression of PCNA and reduced the expression of PTEN, while M-SAT-EX rescued these effects (Fig. 7K). What's more, Angiotensin II (Ang II) and transforming growth factor-β (TGF-β) also play an important role in the proliferation and migration [42, 43]. The data showed that Ang II and TGF-β induced VSMCs proliferation separately, and SAT-derived exosomes and VAT-derived exosomes from obese mice promoted VSMCs proliferation to different extent. As expected, SAT-derived exosomes from obese mice treated with melatonin no longer had the effect of promoting proliferation compared to the SAT-EX group, and VAT-derived exosomes from obese mice treated with melatonin just moderately promoted VSMC proliferation compared to the VAT-EX group (Fig. S13A, B, D, F). Additionally, Ang II enhanced VSMC migration, but TGF-β didn't influence it. Intriguingly, both SAT-EX and VAT-EX variably enhanced the migration of VSMCs in Ang II or TGF-β-induced cell model. Expectedly, treatment with M-SAT-EX didn't affect the migration of VSMC compared to the SAT-EX group, while the proliferation promoting effect of M-VAT-EX was significantly reduced compared with that of VAT-EX (Fig. S13A, C, E, F). Overall, we conclude that melatonin

Fig. 4

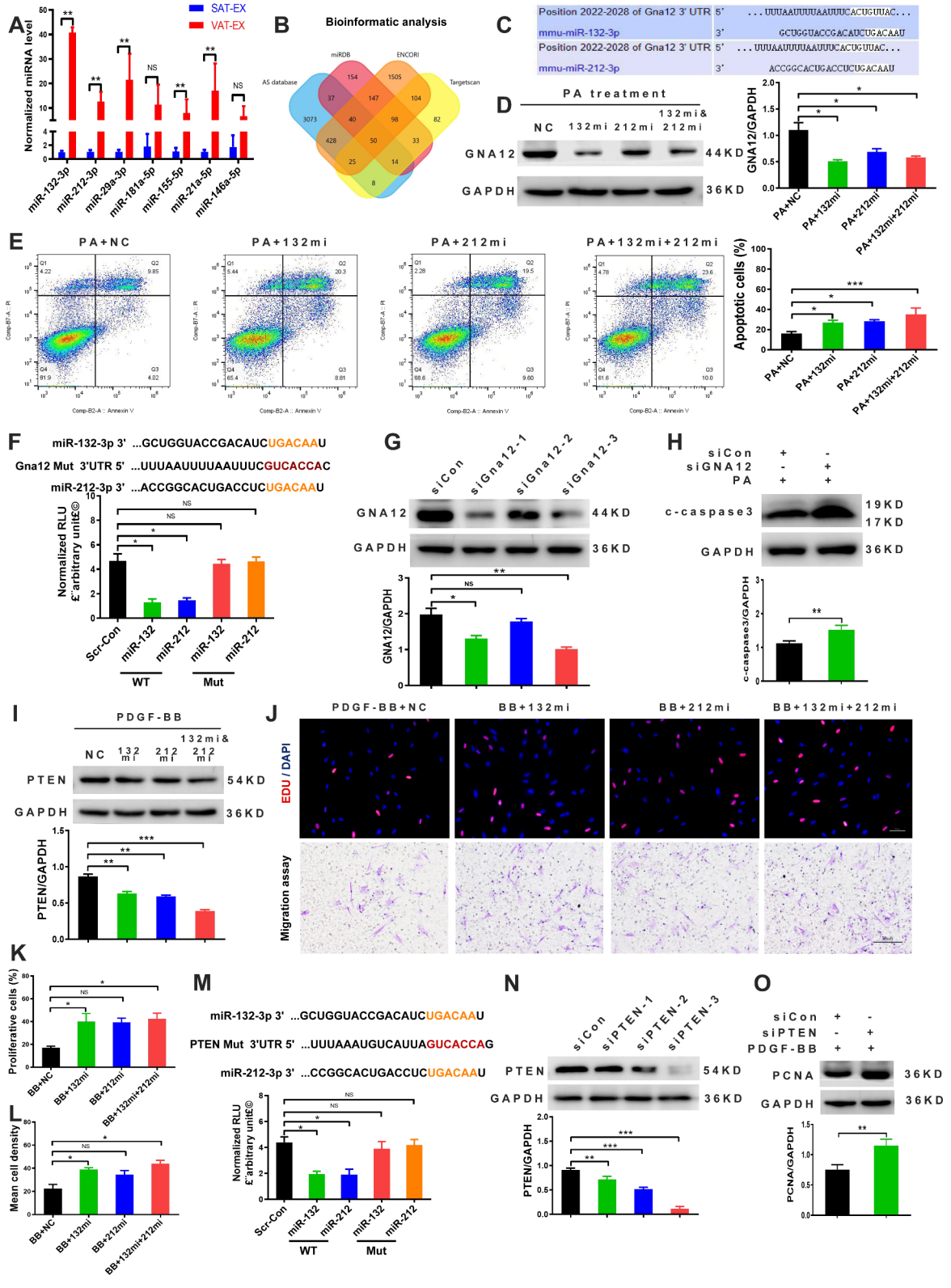

Fig. 4 (See legend on next page.)

(See figure on previous page.)

Fig. 4 The pro-atherosclerotic effect of AT-EX is associated with the MiR-132/212-GNA12/PTEN signaling in vitro. **A** Normalized atherosclerosis-related miRNA levels in SAT-EX and VAT-EX. **B** The potential target genes of the miR-132/212 cluster were predicted by bioinformatic analysis. **C** G protein subunit alpha 12 (Gna12) 3′UTR includes a potential binding site for miR-132-3p and miR-212-3p. **D** GNA12 expression in bEnd.3 after PA treatment for 24 h post-transfection of miR-132 or/and miR-212 mimics, *NC* negative control. **E** Apoptotic bEnd.3 were stained with Annexin V-FITC and PI. **F** The luciferase activity in target cells co-transfected with WT or mutant *Gna12* 3′UTR luciferase constructs and miR-132/212 mimics; Scr-Con, scramble control. **G** Silencing efficiency of small interfering RNA (siRNA) on Gna12. **H** The expression of c-caspase3 in Gna12-silenced bEnd.3. **I** PTEN expression in VSMCs after PDGF-BB treatment for 24 h post-transfection of miR-132 or/and miR-212 mimics. **J** Representative proliferation and migration images of VSMCs. **K**, **L** quantitative analysis of J. (**M**) The luciferase activity in target cells co-transfected with WT or mutant *PTEN* 3′UTR luciferase constructs and miR-132/212 mimics; Scr-Con, scramble control. **N** Silencing efficiency of siRNA on PTEN. **O** The expression of PCNA in PTEN-silenced VSMCs. *NS* no significance, $^{*}P < 0.05$, $^{**}P < 0.01$, $^{***}P < 0.001$, $N = 6$ independent experiments. Data are represented as mean ± SD

regulates the Gna12 signaling in ECs and the PTEN signaling in VSMCs by significantly reducing the miR-132/212 level in VAT exosomes derived from obese mice, thus alleviating atherosclerosis.

Discussion

The main findings of the study include the following: (1) High-fat diet-induced obesity changed the miRNA profile of adipose exosomes, elevating AT exosomal miR-132/212 levels. (2) AT exosomal miR-132/212 exacerbated the progression of atherosclerosis by enhancing endothelial apoptosis, VSMC proliferation and migration within plaques. (3) Treatment with melatonin significantly reduced the levels of miR-132/212 in both SAT and VAT exosomes, thus attenuating the progression of atherosclerosis. (4) The underlying mechanism involves the endothelial miR-132/212-Gna12-Sirtuin 1 axis and the medial miR-132/212-PTEN axis. Overall, melatonin alleviates the initiation and progression of atherosclerosis by regulating the adipose exosomal miRNA profile, deepening our understanding of the pathogenesis of atherosclerosis and providing a new target for its prevention and treatment.

Obesity is associated with an increased susceptibility to cardiovascular diseases [1] and is linked to chronic low-grade inflammation in various tissues [44–49], with a particular emphasis on adipose tissue [50]. Macrophages are identified as the primary inflammatory cells responsible for secreting a significant portion of inflammatory molecules in the adipose tissue of obese individuals [44–49]. Monocytes and macrophages are the predominant cell populations contributing to the upregulation of miR-132/212, in comparison to other immune cells [51] Indeed, our findings reveal a significant enrichment of miR-132/212, especially miR-132, in VAT-EX from obese mice compared to SAT-EX. However, one study reported high expression of miR-155 rather than miR-132/212 in VAT-EX derived from obese mice [16]. This may be attributed to differences in the species and proportions of fatty acids in a high-fat diet, as Yang et al. employed a 45% high-fat diet to induce obesity in mice [16], differing from the 60% high-fat diet utilized in our investigation. As reported in a recent study, the availability of specific fatty acid species determines the direction of disease progression [52].

Endothelial apoptosis is a critical characteristic of vascular injury, closely related with the pathogenesis of atherosclerosis [53]. Our data demonstrate that the enrichment of miR-132/212 in VAT-EX exacerbated endothelial apoptosis in apoE$^{-/-}$ mice, potentially contributing significantly to the progression of atherosclerosis. Similarly, miR-132/212-enriched VAT-EX promoted endothelial apoptosis induced by PA in vitro. Consistent with our findings, prior studies have implicated the miR-132/212 cluster in the vascular inflammatory response [54–56]. Additionally, we revealed Gna12 as the target gene of miR-132/212, and knockdown of Gna12 in endothelial cells effectively mimicked the pro-apoptotic function of miR-132/212. Interestingly, Gna12 was first reported to be involved in atherosclerosis in addition to osteoporosis, tumour, colitis etc. [57–59]. Serving as an upstream regulator, Gna12 stabilized sirtuin 1 protein via transcriptional upregulation of ubiquitin-specific peptidase 22 [60]. Sirtuin 1 exerts protective effects against inflammation, vascular aging, cardiac disorders, and the formation of atherosclerotic plaques [61, 62]. MiR-132/212 directly targets sirtuin 1 [56], and our study demonstrates for the first time that miR-132/212 also target a molecule upstream of SIRT1, resulting in a superposition effect in promoting the development of atherosclerosis. Taken together, our data confirm that the endothelial miR-132/212-Gna12-Sirtuin 1 axis is essential for the deleterious effects of miR-132/212 on atherosclerosis progression, and might play a role in VAT-EX-mediated endothelial apoptosis.

A new study has unveiled that VAT-EX accelerates the progression of atherosclerosis by modulating the formation and polarization of macrophage foam cells [17]. Macrophages are traditionally viewed as the predominant origin of foam cells; however, recent research has revealed that 50–80% of total foam cells originate from SMCs within atherosclerotic plaques [63, 64]. Smooth muscle cells (SMCs) and macrophages undergo proliferation as the intimal lesion progresses, with PDGF stimulating the migration and proliferation of SMCs, subsequently leading to extracellular matrix production within atherosclerotic plaques [1]. Previous studies

Fig. 5

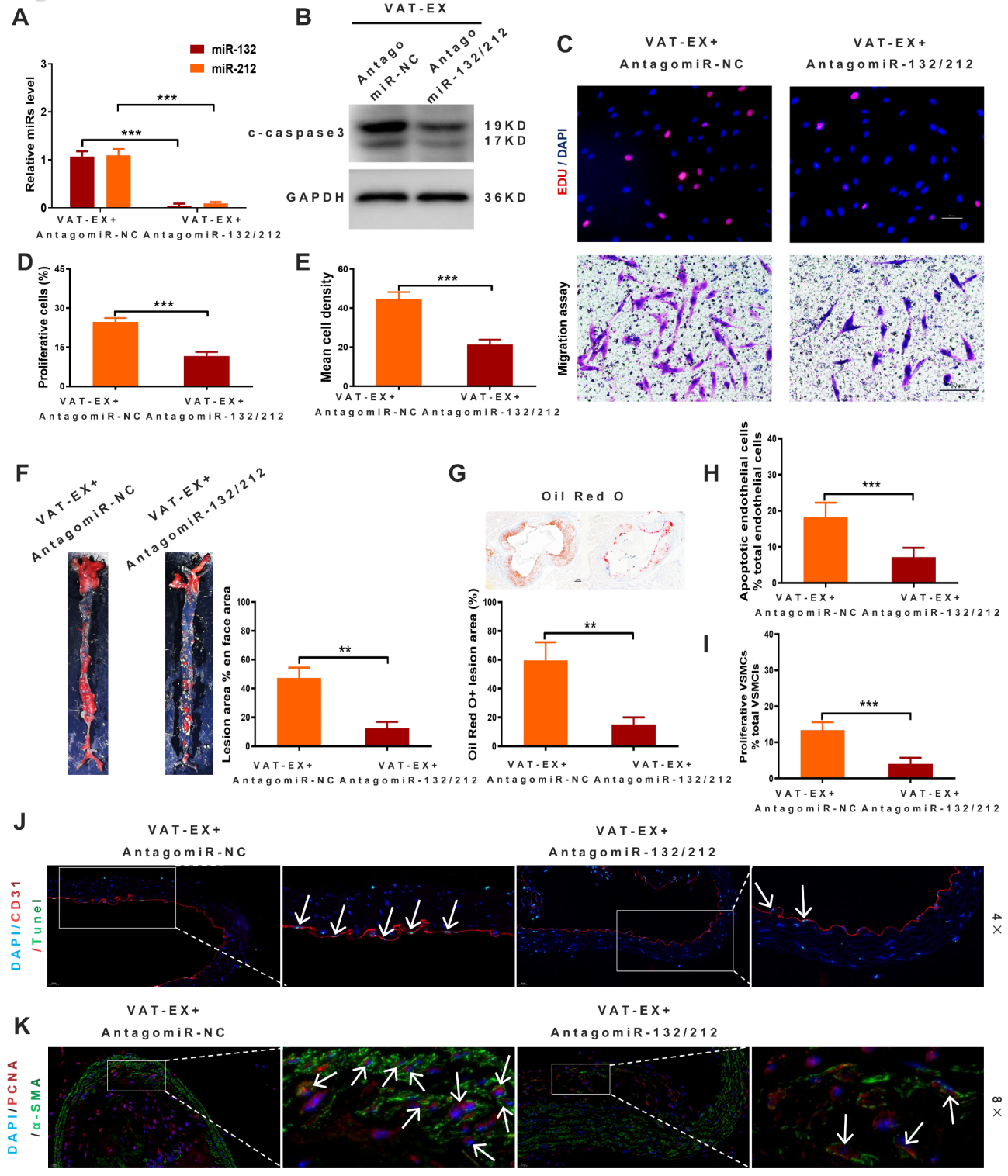

Fig. 5 (See legend on next page.)

(See figure on previous page.)

Fig. 5 AntagomiR-132/212 abolish the pro-atherosclerotic effect of AT-EX in vitro and in vivo. **A** qRT-PCR analysis of miR-132/212 expression in VAT-EX + AntagomiR-132/212. ***$P < 0.001$, $N = 6$ independent experiments. **B** Expression of c-caspase3 in PA-induced bEnd.3 after 12 h of VAT-EX (AntagomiR-NC or AntagomiR-132/212) treatment. **C** Representative proliferation and migration images of primary VSMCs, scale bar = 50 μm. **D** Quantification of proliferation images. **E** Quantification of migration images. **F** Representative images showing Oil Red O staining (red) of neutral lipids in en face atherosclerotic lesions and the quantification, $N = 5$. **G** Representative micrographs showing Oil Red O staining of neutral lipids in the aortic root 300 μm from the aortic sinus and the quantification (scale bar = 200 μm, $N = 5$). **H** The percentage of apoptotic ECs in the thoracic aorta. **I** The percentage of proliferative VSMCs in the thoracic aorta. **J** Representative images of TUNEL (apoptotic cells, green) and CD31 (red) co-staining in sections of thoracic aortas, arrowheads show TUNEL/CD31 co-localization, scale bar = 20 μm, $N = 5$. **K** Representative images of α-SMA (green) and PCNA (red) co-staining in sections of thoracic aortas, arrowheads and dotted line show α-SMA/PCNA co-localization, scale bar = 20 μm, $N = 5$. *NS* no significance, *$P < 0.05$, **$P < 0.01$, ***$P < 0.001$. Data are represented as mean ± SD

have elucidated the role of VAT-EX in enhancing the formation of macrophage foam cells [17]. Our research revealed that miR-132/212-enriched VAT-EX exacerbated the proliferation and migration of SMCs in apoE$^{-/-}$ mice, potentially serving as another crucial factor in the progression of atherosclerosis. Consistent with this, miR-132/212-enriched VAT-EX promoted the migration and proliferation of VSMCs elicited by PDGF-BB in vitro. Multiple studies have indicated that PTEN, a tumor suppressor gene, is targeted by miR-132/212 [37, 38], and silencing of the PTEN gene or specific knockdown in VSMCs enhances VSMCs proliferation and migration [39, 40]. As anticipated, our findings confirm that miR-132/212 targets PTEN, contributing to the atherogenic impact of miR-132/212-enriched VAT-EX. Taken together, these results suggest that in addition to the formation of macrophage foam cells, EC apoptosis and VSMC proliferation and migration play an important synergistic role in the pro-atherogenic encapsulating effect of VAT-EX on miR-132/212.

Melatonin shows potent anti-inflammatory properties in adipose tissue [25, 41]. In obese mice, melatonin treatment led to decreased levels of inflammatory miRNAs, specifically miR-132/212, in VAT-EX. Importantly, we validated that melatonin significantly mitigated the atherogenic effect of VAT-EX from obese mice, at least partly due to the decline in the exosomal miR-132/212 level. Several studies have shown that melatonin confers protection against cardiovascular diseases in animal models, [19] but its efficacy in human studies is limited, [65] possibly because supraphysiological doses are required for therapeutic benefits [66]. Our study suggests a potential role for melatonin in obese patients with atherosclerosis, which warrants validation through extensive clinical trials in the future; It cannot be ignored that the level of miR-29a in exosomes derived from adipose tissue of obese mice is only lower than that of miR132/212 clusters. MiR-29 has been suggested as a potential diagnostic and therapeutic target for cardiovascular diseases [67]. The understanding regarding the upregulation of miR-29a in exosomes as a potential self-protective mechanism activated by the body itself remains unclear. Moreover, SAT-EX from obese mice treated with melatonin demonstrates a beneficial effect in alleviating the initiation and progression of atherosclerosis compared to the vehicle. Consistent with previous studies, SAT and VAT exhibit significant differences in structure and function, [68] while the heterogeneity of intra-depot adipocytes in AT impacts the overall health of adipose tissue. Nevertheless, the identity of the active component enclosed within SAT-EX from melatonin-treated obese mice remains elusive and warrants additional scrutiny. Overall, melatonin administration in obese mice decreased the pro-atherogenic capacity of AT-EX, potentially through the suppression of specific pro-inflammatory miRNAs including miR-132, miR-29a, miR-21, and miR-155.

Conclusion

Obesity changed the miRNA profile of adipose exosomes, then regulating the initiation and progression of atherosclerosis. In addition to atherosclerosis, adipose exosomes, as a new type of adipokines, also regulate the development of other diseases, which still need further research.

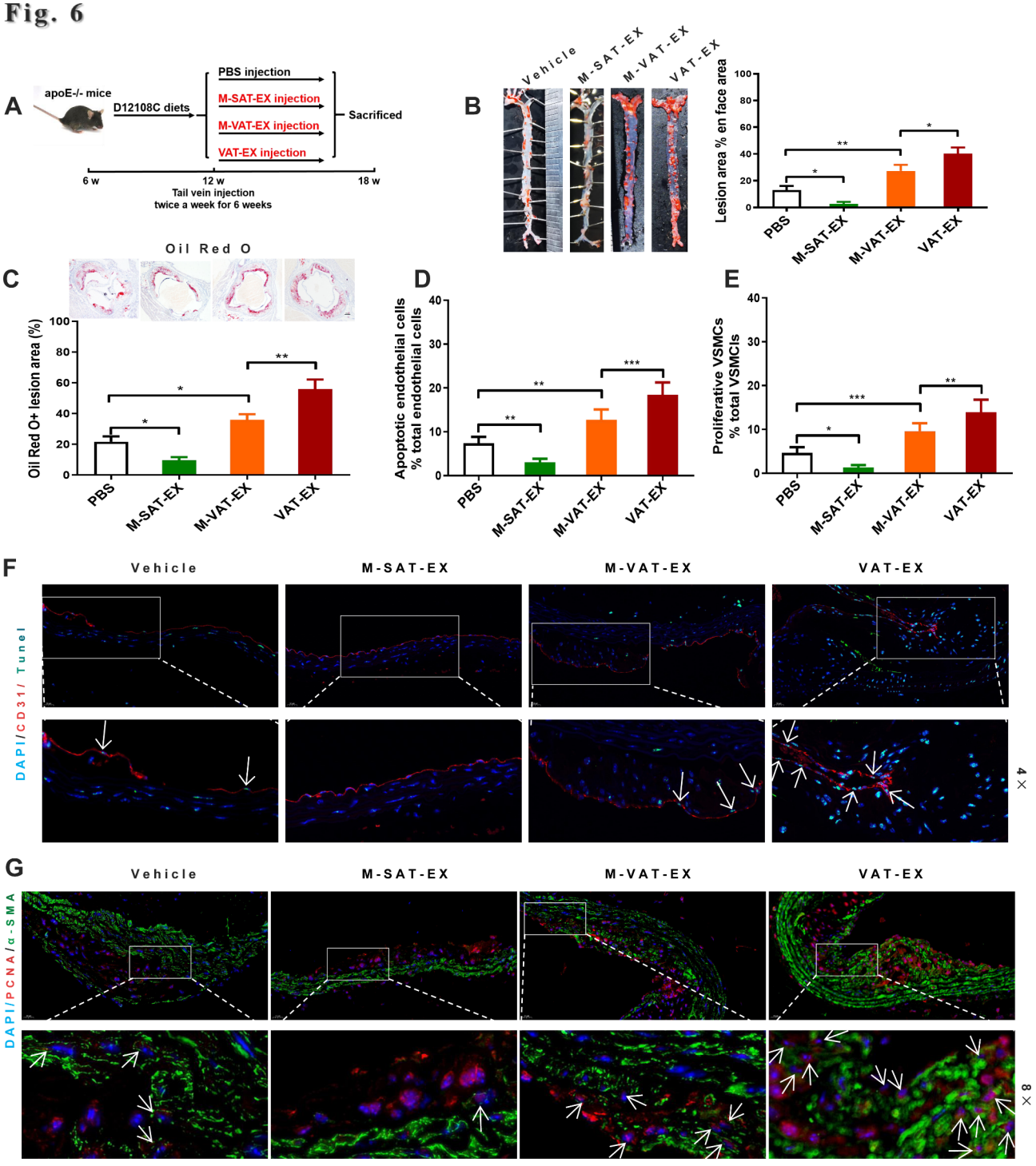

Fig. 6 Melatonin alleviates the pro-atherosclerotic effect of at exosomes derived from obese mice and modulates miR-132/212-GNA12/PTEN signaling in apoE$^{-/-}$ mice. **A** The animal experimental procedure for detecting the effects of SAT-EX and VAT-EX after melatonin intervention (M-SAT-EX, M-VAT-EX) for one month on AS. **B** Representative images showing Oil Red O staining (red) of neutral lipids in en face atherosclerotic lesions and the quantitative analysis, $N = 6$. **C** Representative micrographs showing Oil Red O staining in the aortic root 300 μm from the aortic sinus and the quantitative analysis, scale bar = 200 μm, $N = 6$. **D** the percentage of apoptotic ECs in the thoracic aorta. **E** The percentage of proliferative VSMCs in the thoracic aorta. **F** Representative images of TUNEL (green) and CD31 (red) co-staining in sections of thoracic aortas, arrowheads show TUNEL/CD31 co-localization, scale bar = 20 μm, $N = 6$. **G** Representative images of α-SMA (green) and PCNA (red) co-staining in sections of thoracic aortas, arrowheads and dotted line show α-SMA/PCNA co-localization, scale bar = 20 μm, $N = 5$. *NS* no significance, $^{*}P < 0.05$, $^{**}P < 0.01$, $^{***}P < 0.001$. Data are represented as mean ± SD

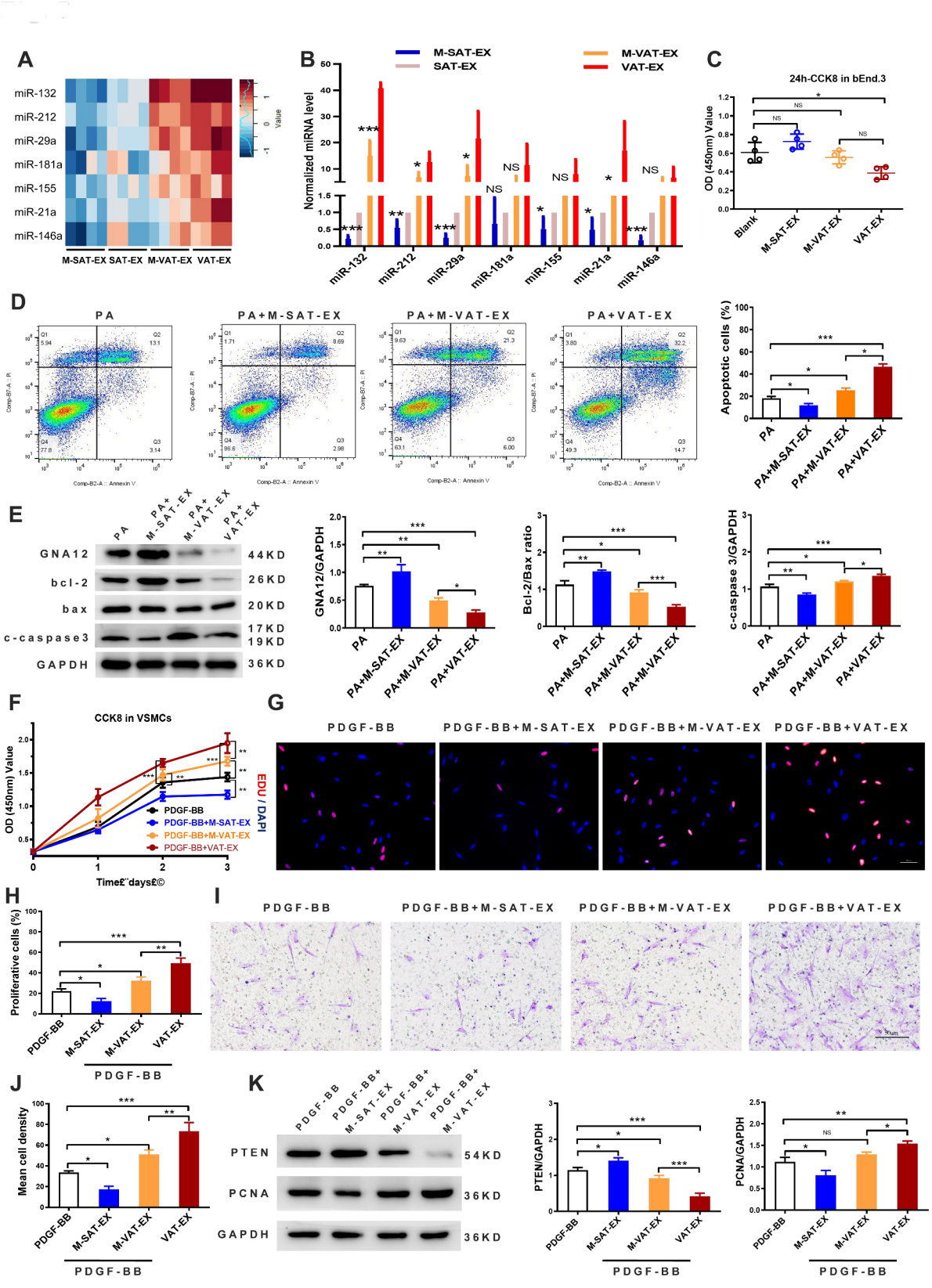

Fig. 7 (See legend on next page.)

(See figure on previous page.)

Fig. 7 The endothelial miR-132/212-Gna12 axis and medial miR-132/212-PTEN axis are essential for the effects of AT-EX on atherosclerosis. **A** Heat map depicting changes in atherosclerosis-relevant microRNAs in four kinds of exosomes. **B** The miRNAs level in four kinds of exosomes examined by qRT-PCR assay, taking SAT-EX data as reference. M-SAT-EX vs. SAT-EX, M-VAT-EX vs. VAT-EX. **C** Effect of M-SAT-EX and M-VAT-EX on the viability of bEnd.3 at 24 h. **D** Apoptotic bEnd.3 were stained with Annexin V-FITC and PI. **E** Expression of GNA12, BCL-2, Bax and c-caspase3 in PA-induced bEnd.3 after SAT-EX or VAT-EX treatment. **F** Effect of M-SAT-EX and M-VAT-EX on the viability of primary VSMCs. **G** Representative proliferation images of primary VSMCs, scale bar = 50 μm. **H** uantitative analysis of G. **I** Representative migration images of primary VSMCs, scale bar = 50 μm. **J** Quantitative analysis of I. **K** Expression of PTEN and PCNA in PDGF-BB-induced primary VSMCs after M-SAT-EX or M-VAT-EX treatment. *NS* no significance, *$P < 0.05$, **$P < 0.01$, ***$P < 0.001$, $N = 6$ independent experiments. Data are represented as mean ± SD

Abbreviations

Ang II	Angiotensin II
AT-EX	Adipose tissue-derived exosomes
CCK-8	Cell counting kit-8
DIO	Diet-induced obesity
FBS	Foetal bovine serum
Gna12	G protein subunit alpha 12
HFD	High-fat diet
miR-132/212	MicroRNA-132/212
M-VAT-EX	VAT-derived exosomes from obese mice treated with melatonin
NC	Normal chow
PA	Palmitate acid
PDGF-BB	Platelet-derived growth factor type BB
PTEN	Phosphatase and tensin homolog
SAT	Subcutaneous adipose tissue
M-SAT-EX	SAT-derived exosomes from obese mice treated with melatonin
TGF-β	Transforming growth factor-β
VAT	Visceral adipose tissue
VSMCs	Vascular smooth muscle cells

Supplementary Information

The online version contains supplementary material available at https://doi.org/10.1186/s12933-024-02404-x.

Supplementary Material 1

Acknowledgements
We express our sincere gratitude to Zhuang TongTian for his invaluable assistance.

Author contributions
Conceptualization: L.Q.Y., B.G.; methodology: F.X., X.L., F.W., F.X.Z.L.; investigation: L.Q.Y., B.G.; visualization: C.C.L., S.K.S., M.H.Z., Y.W., Q.S.X., L.M.L., Z.A.Z., K.X.T., W.L.O.Y., J.Y.D., Y.Y.W., M.H.E.U., Y.C.C.; supervision: T.T.Z., F.X.; writing—original draft: B.G., T.T.Z.; writing—review & editing: L.Q.Y., F.X., X.B.L.

Funding
This study was supported by National Natural Science Foundation of China (No. 82370892, 82070910, 82100944, 82200869 and 82100494), the National Key Research & Development Program (No. 2021YFC2501701), National Clinical Key Specialties Major Research Projects (Z2023026). The Health Research Project in Hunan Province (No. 20231696, 202103062278), Health Research Project of Hunan Provincial Health Commission (W20243019), the Natural Science Foundation of Hunan Province (No. 2022JJ40721, 2022JJ40715) and National Undergraduate Innovation Training Program of Central South University (Project Number: 2022105330213 and 2022105330235).

Data availability
No datasets were generated or analysed during the current study.

Declarations

Ethics approval and consent to participate
All animal experiments comply with the ARRIVE guidelines.

Consent for publication
All authors consent for the publication of this study.

Competing interests
The authors declare no competing interests.

Author details
[1]National Clinical Research Center for Metabolic Diseases, Department of Metabolism and Endocrinology, The Second Xiangya Hospital, Central South University, Changsha 410000, China
[2]Department of Metabolism and Endocrinology, General Hospital of Northern Theater Command, Shenyang 110016, China
[3]Department of Dermatology, Air Force Hospital of Northern Theater Command, Shenyang, China
[4]Department of Radiology, The Second Xiangya Hospital, Central South University, Changsha, Hunan, People's Republic of China
[5]Department of Pathology, The Second Xiangya Hospital, Central South University, Changsha, Hunan, People's Republic of China
[6]Department of Cardiovascular Surgery, The Second Xiangya Hospital, Central South University, Changsha, Hunan, People's Republic of China

Received: 27 January 2024 / Accepted: 14 August 2024
Published online: 09 September 2024

References

1. Libby P. The changing landscape of atherosclerosis. Nature. 2021;592:524–33.
2. Fuster JJ, Ouchi N, Gokce N, Walsh K. Obesity-induced changes in adipose tissue microenvironment and their impact on cardiovascular disease. Circ Res. 2016;118:1786–807.
3. Francisco V, Pino J, Gonzalez-Gay MA, Lago F, Karppinen J, Tervonen O, Mobasheri A, Gualillo O. A new immunometabolic perspective of intervertebral disc degeneration. Nat Rev Rheumatol. 2022;18:47–60.
4. Hiuge-Shimizu A, Kishida K, Funahashi T, Ishizaka Y, Oka R, Okada M, Suzuki S, Takaya N, Nakagawa T, Fukui T, Fukuda H, Watanabe N, Yoshizumi T, Nakamura T, Matsuzawa Y, Yamakado M, Shimomura I. Absolute value of visceral fat area measured on computed tomography scans and obesity-related cardiovascular risk factors in large-scale Japanese general population (the VACATION-J study). Ann Med. 2012;44:82–92.
5. Neeland IJ, Ross R, Despres JP, Matsuzawa Y, Yamashita S, Shai I, Seidell J, Magni P, Santos RD, Arsenault B, Cuevas A, Hu FB, Griffin B, Zambon A, Barter P, Fruchart JC, Eckel RH. Visceral and ectopic fat, atherosclerosis, and cardiometabolic disease: a position statement. Lancet Diabetes Endocrinol. 2019;7:715–25.
6. Kalluri R, LeBleu VS. The biology, function, and biomedical applications of exosomes. Science. 2020;367:eaau6977.
7. Pan Y, Hui X, Hoo R, Ye D, Chan C, Feng T, Wang Y, Lam K, Xu A. Adipocyte-secreted exosomal microRNA-34a inhibits M2 macrophage polarization to promote obesity-induced adipose inflammation. J Clin Invest. 2019;129:834–49.
8. Xing X, Li Z, Yang X, Li M, Liu C, Pang Y, Zhang L, Li X, Liu G, Xiao Y. Adipose-derived mesenchymal stem cells-derived exosome-mediated microRNA-342-5p protects endothelial cells against atherosclerosis. Aging. 2020;12:3880–98.
9. Ying W, Riopel M, Bandyopadhyay G, Dong Y, Birmingham A, Seo JB, Ofrecio JM, Wollam J, Hernandez-Carretero A, Fu W, Li P, Olefsky JM. Adipose tissue macrophage-derived exosomal miRNAs can modulate in vivo and in vitro insulin sensitivity. Cell. 2017;171:372–84.
10. Scheja L, Heeren J. The endocrine function of adipose tissues in health and cardiometabolic disease. Nat Rev Endocrinol. 2019;15:507–24.

11. Halberg N, Wernstedt-Asterholm I, Scherer PE. The adipocyte as an endocrine cell. Endocrinol Metab Clin North Am. 2008;37:753–68.
12. Kita S, Maeda N, Shimomura I. Interorgan communication by exosomes, adipose tissue, and adiponectin in metabolic syndrome. J Clin Invest. 2019;129:4041–9.
13. Thomou T, Mori MA, Dreyfuss JM, Konishi M, Sakaguchi M, Wolfrum C, Rao TN, Winnay JN, Garcia-Martin R, Grinspoon SK, Gorden P, Kahn CR. Adipose-derived circulating miRNAs regulate gene expression in other tissues. Nature. 2017;542:450–5.
14. Crewe C, Joffin N, Rutkowski JM, Kim M, Zhang F, Towler DA, Gordillo R, Scherer PE. An endothelial-to-adipocyte extracellular vesicle axis governed by metabolic state. Cell. 2018;175:695–708.
15. Zhou X, Li Z, Qi M, Zhao P, Duan Y, Yang G, Yuan L. Brown adipose tissue-derived exosomes mitigate the metabolic syndrome in high fat diet mice. Theranostics. 2020;10:8197–210.
16. Wei M, Gao X, Liu L, Li Z, Wan Z, Dong Y, Chen X, Niu Y, Zhang J, Yang G. Visceral adipose tissue derived exosomes exacerbate colitis severity via pro-inflammatory MiRNAs in high fat diet fed mice. ACS Nano. 2020;14:5099–110.
17. Xie Z, Wang X, Liu X, Du H, Sun C, Shao X, Tian J, Gu X, Wang H, Tian J, Yu B. Adipose-derived exosomes exert proatherogenic effects by regulating macrophage foam cell formation and polarization. J Am Heart Assoc. 2018;7:e007442.
18. Short RV. Melatonin. BMJ. 1993;307:952–3.
19. Tengattini S, Reiter RJ, Tan DX, Terron MP, Rodella LF, Rezzani R. Cardiovascular diseases: protective effects of melatonin. J Pineal Res. 2008;44:16–25.
20. Zhou H, Ma Q, Zhu P, Ren J, Reiter RJ, Chen Y. Protective role of melatonin in cardiac ischemia-reperfusion injury: from pathogenesis to targeted therapy. J Pineal Res. 2018;64:e12471.
21. Zhang Y, Liu X, Bai X, Lin Y, Li Z, Fu J, Li M, Zhao T, Yang H, Xu R, Li J, Ju J, Cai B, Xu C, Yang B. Melatonin prevents endothelial cell pyroptosis via regulation of long noncoding RNA MEG3/miR-223/NLRP3 axis. J Pineal Res. 2018;64:e12449.
22. Ekmekcioglu C, Haslmayer P, Philipp C, Mehrabi MR, Glogar HD, Grimm M, Thalhammer T, Marktl W. 24 h variation in the expression of the mt1 melatonin receptor subtype in coronary arteries derived from patients with coronary heart disease. Chronobiol Int. 2001;18:973–85.
23. Ekmekcioglu C, Thalhammer T, Humpeler S, Mehrabi MR, Glogar HD, Holzenbein T, Markovic O, Leibetseder VJ, Strauss-Blasche G, Marktl W. The melatonin receptor subtype MT2 is present in the human cardiovascular system. J Pineal Res. 2003;35:40–4.
24. Karamitri A, Jockers R. Melatonin in type 2 diabetes mellitus and obesity. Nat Rev Endocrinol. 2019;15:105–25.
25. Liu Z, Gan L, Zhang T, Ren Q, Sun C. Melatonin alleviates adipose inflammation through elevating alpha-ketoglutarate and diverting adipose-derived exosomes to macrophages in mice. J Pineal Res. 2018;64:e124545.
26. Li FX, Liu JJ, Xu F, Shan SK, Zheng MH, Lei LM, Lin X, Guo B, Li CC, Wu F, Tang KX, Cao YC, Wu YY, Duan JY, Wu YL, He SY, Chen X, Yuan LQ. Cold exposure protects against medial arterial calcification development via autophagy. J Nanobiotechnol. 2023;21:226.
27. Liu Y, Sun Y, Lin X, Zhang D, Hu C, Liu J, Zhu Y, Gao A, Han H, Chai M, Zhang J, Zhou Y, Zhao Y. Perivascular adipose-derived exosomes reduce foam cell formation by regulating expression of cholesterol transporters. Front Cardiovasc Med. 2021;8:697510.
28. Meng B, Li Y, Ding Y, Xu X, Wang L, Guo B, Zhu B, Zhang J, Xiang L, Dong J, Liu M, Xiang L, Xiang G. Myeloid-derived growth factor inhibits inflammation and alleviates endothelial injury and atherosclerosis in mice. Sci Adv. 2021;7:eabe6903.
29. Li X, Gonzalez O, Shen X, Barnhart S, Kramer F, Kanter JE, Vivekanandan-Giri A, Tsuchiya K, Handa P, Pennathur S, Kim F, Coleman RA, Schaffer JE, Bornfeldt KE. Endothelial acyl-CoA synthetase 1 is not required for inflammatory and apoptotic effects of a saturated fatty acid-rich environment. Arterioscler Thromb Vasc Biol. 2013;33:232–40.
30. Mao Y, Luo W, Zhang L, Wu W, Yuan L, Xu H, Song J, Fujiwara K, Abe JI, LeMaire SA, Wang XL, Shen YH. STING-IRF3 triggers endothelial inflammation in response to free fatty acid-induced mitochondrial damage in diet-induced obesity. Arterioscler Thromb Vasc Biol. 2017;37:920–9.
31. Hulsmans M, Holvoet P. MicroRNA-containing microvesicles regulating inflammation in association with atherosclerotic disease. Cardiovasc Res. 2013;100:7–18.
32. Li D, Wang A, Liu X, Meisgen F, Grunler J, Botusan IR, Narayanan S, Erikci E, Li X, Blomqvist L, Du L, Pivarcsi A, Sonkoly E, Chowdhury K, Catrina SB, Stahle M, Landen NX. MicroRNA-132 enhances transition from inflammation to proliferation during wound healing. J Clin Invest. 2015;125:3008–26.
33. Ma F, Xu S, Liu X, Zhang Q, Xu X, Liu M, Hua M, Li N, Yao H, Cao X. The microRNA miR-29 controls innate and adaptive immune responses to intracellular bacterial infection by targeting interferon-gamma. Nat Immunol. 2011;12:861–9.
34. Sun X, Sit A, Feinberg MW. Role of miR-181 family in regulating vascular inflammation and immunity. Trends Cardiovasc Med. 2014;24:105–12.
35. Olivieri F, Prattichizzo F, Giuliani A, Matacchione G, Rippo MR, Sabbatinelli J, Bonafe M. miR-21 and miR-146a: the microRNAs of inflammaging and age-related diseases. Ageing Res Rev. 2021;70:101374.
36. de la Rica L, Garcia-Gomez A, Comet NR, Rodriguez-Ubreva J, Ciudad L, Vento-Tormo R, Company C, Alvarez-Errico D, Garcia M, Gomez-Vaquero C, Ballestar E. NF-kappaB-direct activation of microRNAs with repressive effects on monocyte-specific genes is critical for osteoclast differentiation. Genome Biol. 2015;16:2.
37. Jin W, Reddy MA, Chen Z, Putta S, Lanting L, Kato M, Park JT, Chandra M, Wang C, Tangirala RK, Natarajan R. Small RNA sequencing reveals microRNAs that modulate angiotensin II effects in vascular smooth muscle cells. J Biol Chem. 2012;287:15672–83.
38. Mziaut H, Henniger G, Ganss K, Hempel S, Wolk S, McChord J, Chowdhury K, Ravassard P, Knoch KP, Krautz C, Weitz J, Grutzmann R, Pilarsky C, Solimena M, Kersting S. MiR-132 controls pancreatic beta cell proliferation and survival through Pten/Akt/Foxo3 signaling. Mol Metab. 2020;31:150–62.
39. Huang J, Kontos CD. Inhibition of vascular smooth muscle cell proliferation, migration, and survival by the tumor suppressor protein PTEN. Arterioscler Thromb Vasc Biol. 2002;22:745–51.
40. Chen WJ, Lin KH, Lai YJ, Yang SH, Pang JH. Protective effect of propylthiouracil independent of its hypothyroid effect on atherogenesis in cholesterol-fed rabbits: PTEN induction and inhibition of vascular smooth muscle cell proliferation and migration. Circulation. 2004;110:1313–9.
41. Liu Z, Gan L, Xu Y, Luo D, Ren Q, Wu S, Sun C. Melatonin alleviates inflammasome-induced pyroptosis through inhibiting NF-kappaB/GSDMD signal in mice adipose tissue. J Pineal Res. 2017;63:e12414.
42. He X, Deng J, Yu XJ, Yang S, Yang Y, Zang WJ. Activation of M3AChR (type 3 muscarinic acetylcholine receptor) and Nrf2 (nuclear factor erythroid 2-Related factor 2) signaling by choline alleviates vascular smooth muscle cell phenotypic switching and vascular remodeling. Arterioscler Thromb Vasc Biol. 2020;40:2649–64.
43. Lim WW, Dong J, Ng B, Widjaja AA, Xie C, Su L, Kwek XY, Tee N, Jian PC, Schafer S, Viswanathan S, Cook SA. Inhibition of IL11 signaling reduces aortic pathology in murine marfan syndrome. Circ Res. 2022;130:728–40.
44. Saltiel AR, Olefsky JM. Inflammatory mechanisms linking obesity and metabolic disease. J Clin Invest. 2017;127:1–4.
45. McNelis JC, Olefsky JM. Macrophages, immunity, and metabolic disease. Immunity. 2014;41:36–48.
46. Hotamisligil GS. Inflammation, metaflammation and immunometabolic disorders. Nature. 2017;542:177–85.
47. Wu H, Ballantyne CM. Skeletal muscle inflammation and insulin resistance in obesity. J Clin Invest. 2017;127:43–54.
48. Lackey DE, Olefsky JM. Regulation of metabolism by the innate immune system. Nat Rev Endocrinol. 2016;12:15–28.
49. McLaughlin T, Ackerman SE, Shen L, Engleman E. Role of innate and adaptive immunity in obesity-associated metabolic disease. J Clin Invest. 2017;127:5–13.
50. Wu H, Ballantyne CM. Metabolic inflammation and insulin resistance in obesity. Circ Res. 2020;126:1549–64.
51. Wanet A, Tacheny A, Arnould T, Renard P. miR-212/132 expression and functions: within and beyond the neuronal compartment. Nucleic Acids Res. 2012;40:4742–53.
52. Lien EC, Westermark AM, Zhang Y, Yuan C, Li Z, Lau AN, Sapp KM, Wolpin BM, Vander HM. Low glycaemic diets alter lipid metabolism to influence tumour growth. Nature. 2021;599:302–7.
53. Xu S, Ilyas I, Little PJ, Li H, Kamato D, Zheng X, Luo S, Li Z, Liu P, Han J, Harding IC, Ebong EE, Cameron SJ, Stewart AG, Weng J. Endothelial dysfunction in atherosclerotic cardiovascular diseases and beyond: from mechanism to pharmacotherapies. Pharmacol Rev. 2021;73:924–67.
54. Kumarswamy R, Volkmann I, Beermann J, Napp LC, Jabs O, Bhayadia R, Melk A, Ucar A, Chowdhury K, Lorenzen JM, Gupta SK, Batkai S, Thum T. Vascular importance of the miR-212/132 cluster. Eur Heart J. 2014;35:3224–31.
55. Zhang L, Huang D, Wang Q, Shen D, Wang Y, Chen B, Zhang J, Gai L. MiR-132 inhibits expression of SIRT1 and induces pro-inflammatory processes of

vascular endothelial inflammation through blockade of the SREBP-1c metabolic pathway. Cardiovasc Drugs Ther. 2014;28:303–11.
56. Kong P, Yu Y, Wang L, Dou YQ, Zhang XH, Cui Y, Wang HY, Yong YT, Liu YB, Hu HJ, Cui W, Sun SG, Li BH, Zhang F, Han M. circ-Sirt1 controls NF-kappaB activation via sequence-specific interaction and enhancement of SIRT1 expression by binding to miR-132/212 in vascular smooth muscle cells. Nucleic Acids Res. 2019;47:3580–93.
57. Lees CW, Barrett JC, Parkes M, Satsangi J. New IBD genetics: common pathways with other diseases. Gut. 2011;60:1739–53.
58. Mullin BH, Tickner J, Zhu K, Kenny J, Mullin S, Brown SJ, Dudbridge F, Pavlos NJ, Mocarski ES, Walsh JP, Xu J, Wilson SG. Characterisation of genetic regulatory effects for osteoporosis risk variants in human osteoclasts. Genome Biol. 2020;21:80.
59. Rasheed S, Subramanyan LV, Lim WK, Udayappan UK, Wang M, Casey PJ. The emerging roles of Galpha12/13 proteins on the hallmarks of cancer in solid tumors. Oncogene. 2022;41:147–58.
60. Kim TH, Yang YM, Han CY, Koo JH, Oh H, Kim SS, You BH, Choi YH, Park TS, Lee CH, Kurose H, Noureddin M, Seki E, Wan YY, Choi CS, Kim SG. Galpha12 ablation exacerbates liver steatosis and obesity by suppressing USP22/SIRT1-regulated mitochondrial respiration. J Clin Invest. 2018;128:5587–602.
61. Kane AE, Sinclair DA. Sirtuins and NAD(+) in the development and treatment of metabolic and cardiovascular diseases. Circ Res. 2018;123:868–85.
62. D'Onofrio N, Servillo L, Balestrieri ML. SIRT1 and SIRT6 signaling pathways in cardiovascular disease protection. Antioxid Redox Signal. 2018;28:711–32.
63. Shankman LS, Gomez D, Cherepanova OA, Salmon M, Alencar GF, Haskins RM, Swiatlowska P, Newman AA, Greene ES, Straub AC, Isakson B, Randolph GJ, Owens GK. KLF4-dependent phenotypic modulation of smooth muscle cells has a key role in atherosclerotic plaque pathogenesis. Nat Med. 2015;21:628–37.
64. Allahverdian S, Chehroudi AC, McManus BM, Abraham T, Francis GA. Contribution of intimal smooth muscle cells to cholesterol accumulation and macrophage-like cells in human atherosclerosis. Circulation. 2014;129:1551–9.
65. Nabavi SM, Nabavi SF, Sureda A, Xiao J, Dehpour AR, Shirooie S, Silva AS, Baldi A, Khan H, Daglia M. Anti-inflammatory effects of melatonin: a mechanistic review. Crit Rev Food Sci Nutr. 2019;59:S4–16.
66. Duell PB, Wheaton DL, Shultz A, Nguyen H. Inhibition of LDL oxidation by melatonin requires supraphysiologic concentrations. Clin Chem. 1998;44:1931–6.
67. Liu MN, Luo G, Gao WJ, Yang SJ, Zhou H. miR-29 family: a potential therapeutic target for cardiovascular disease. Pharmacol Res. 2021;166:105510.
68. Ibrahim MM. Subcutaneous and visceral adipose tissue: structural and functional differences. Obes Rev. 2010;11:11–8.

Publisher's note